

Wavelength Selective Optical Logic and Interconnects

M. Selim Ünlü, *Member, IEEE*, Samuel Strite, A. Levent Demirel, *Student Member, IEEE*, Serdar Taşiran, A. Salvador, and Hadis Morkoç, *Fellow, IEEE*

Abstract—We describe a novel wavelength selective optical logic (WSOL) element which makes use of monolithically integrated wavelength selective optical input and output elements. Input optical signals are detected by photothyristors situated in an optical cavity which provides a highly selective response at a wavelength determined by the fabrication process. Output signals are generated by vertical cavity surface emitting lasers whose lasing wavelengths can also be specified during the fabrication process. We propose a vertical integration of these input and output elements which will be highly suitable for wavelength selective optical logic and wavelength selective optical interconnect applications. These devices can be fabricated to detect and emit within independently selected narrow wavelength ranges, at arbitrarily chosen positions across the wafer. The broad tunability range and the high wavelength selectivity of each WSOL device allows a large number of wavelengths to be used simultaneously while low crosstalk is maintained between nearby devices. As interconnects, the WSOL input and output elements will allow the information from many closely spaced wavelength channels to be coupled through a single optical fiber. As individual logic elements, WSOL devices are capable of completely optical logic operations at designer selected input and output wavelengths. The proposed circuitry is easily cascadable so that arbitrarily complex optical logic functions can be performed by WSOL devices in series. Several of the possible logic functions are described including OR and AND gates, an ADDER, and a FLIP-FLOP.

I. INTRODUCTION

RECENTLY, interest in new device technologies for digital optoelectronic circuits has been mounting [1]–[4]. Optical interconnects and switches are considered as necessary elements for optical signal processing and digital communication systems. With these applications in mind, many researchers have demonstrated optoelectronic switches [5]–[11] whose operational principles are similar to or based on the Schockley diode [10], [12]–[14]. However, all of these schemes are limited by their broad-band input and/or output response which limits the number of channels that can be coupled through a single optical fiber and makes the system susceptible to significant amounts of crosstalk between neighboring devices.

Manuscript received February 7, 1992; revised August 27, 1992. This work was supported by the Office of Naval Research under Contract N00014-88-K-0724. The work of S. Strite was supported by an AFOSR Fellowship.

M. Selim Ünlü is with the Department of Electrical, Computer, and Systems Engineering, Boston University, Boston, MA 02215.

S. Strite, A. L. Demirel, A. Salvador, and H. Morkoç are with the Coordinated Science Laboratory, University of Illinois, Urbana, IL 61801.

S. Taşiran is with the Electrical Engineering Department, University of California, Berkeley, CA.

IEEE Log Number 9205906.

In this paper, we describe a novel wavelength selective optical logic (WSOL) device which makes use of monolithically integrated wavelength selective optical inputs and output elements. Photothyristors situated in an optical cavity provide a highly selective response to optical inputs at a wavelength determined during the fabrication. Vertical cavity surface emitting lasers (VCSEL), whose lasing wavelengths can be tuned over a fairly broad range, also determined by the fabrication process, provide a monochromatic output signal. We propose a vertical integration of these input and output elements which is very likely to be highly suitable for optical interconnect and optical logic applications. WSOL devices can be fabricated to detect and emit within narrow bandwidths (not necessarily the same) at arbitrarily chosen positions across the wafer providing multiple wavelength operation in the vicinity of a center wavelength. The WSOL devices, when used as optical interconnects, will allow the information from a number of closely spaced wavelength channels to be coupled through a single optical fiber. As logic elements, the WSOL device is suitable for optoelectronic integrated circuits due to the flexibility provided by multiple wavelength operation. Its ability to use the input and output wavelengths as variables, its inherent cascability, and the low crosstalk between adjacent devices resulting from the wavelength selectivity of each device are the trademarks of this device.

The paper is divided into sections which introduce the fundamentals of operation principles and wavelength selectivity of the optoelectronic switching devices coupled with the proposed multiple wavelength VCSEL arrays to form the WSOL device. The discussion begins by describing the crystal growth and device fabrication technique. The operational principles and performance of the photothyristor optical switch and detector are presented, including a scheme which enables such a device to discriminate between two distinct wavelength optical inputs and perform simple logic functions. We then review the resonant cavity effect which enables the response of devices situated within the optical cavity to be made highly wavelength selective in a narrow band whose wavelength is determined during the fabrication process. A fabrication technique based on the phase tuning of a hybrid mirror, formed by a combination of a metal reflector and a quarter-wave stack, is proposed for producing multiple wavelength VCSEL arrays. We continue by envisioning a monolithically integrated photothyristor detector and VCSEL output combined in a vertical scheme on a single

wafer without the need for regrowth. Conventional fabrication techniques which can easily form wavelength selective optical interconnects and WSOL elements from these layers are described. Finally, simple logic operations which can be performed by these elements are described and possible applications of this novel wavelength selective multiple channel optical logic are proposed.

II. DEVICE GROWTH AND FABRICATION

The structures that were implemented were all grown using a Perkin Elmer 430 molecular beam epitaxy (MBE) system on GaAs (001) substrates. GaAs and AlGaAs layers were grown at $1 \mu\text{m/h}$ at 580 and 610°C , respectively, while InGaAs layers were grown at $0.6 \mu\text{m/h}$ at 540°C . Quarter-wave GaAs-AlAs mirrors were deposited at 600°C using a $1 \mu\text{m/h}$ GaAs growth rate and a $0.3 \mu\text{m/h}$ AlAs growth rate. Standard photolithography and wet etching techniques were used to fabricate devices with various emitter sizes for electrical characterization. Circular devices with emitter windows were also fabricated for optical measurements. Contacts to n- and p-type layers were made by AuGe-Ni-Au and AuBe evaporations, respectively.

III. OPERATIONAL PRINCIPLES OF THE PHOTOTHYRISTOR

A thyristor is an n-p-n-p Schockley diode fabricated in a three terminal configuration. In the case of the photothyristor, the function of electrical base contact is replaced by an optical excitation. For a complete understanding of the optical switches described in this paper, a knowledge of the electrical switching characteristics of the Schockley diode is essential. The investigated structures incorporate an AlGaAs-GaAs heterojunction (N-p-n-p) to improve the injection efficiency of the base-emitter junction and InGaAs quantum wells at the n-p junction to improve carrier confinement and obtain light beyond the absorption limit of the GaAs substrate. The structure resembles a heterojunction bipolar transistor (HBT) vertically integrated with a light emitting diode (LED). Fig. 1 gives the schematic layer structure (a) and the band diagram (b) of the device (HBT-LED) showing the various OFF state current components. The HBT-LED can be viewed as an interwoven N-p-n AlGaAs-GaAs HBT and a p-n-p GaAs bipolar transistor. The base of the one is the collector of the other.

The common-emitter current-voltage (I - V) characteristics of the device are given in Fig. 2(a) and (b) for constant base current (I_B) steps and for constant base-emitter voltage (V_{BE}) steps, respectively. As can be seen from Fig. 2(a), the device functions as a normal HBT is the low current regime (OFF state). We should note that the collector current is supplied by holes injected from the p^+ -substrate (I_{pS}). The electron current injected from the emitter into the collector of the N-p-n transistor (I_{nC}) recombines with the holes (I_{pS}) provided by the p-n-p device in the InGaAs quantum wells generating light [Fig. 1(b)]. The holes from the substrate which do not recom-

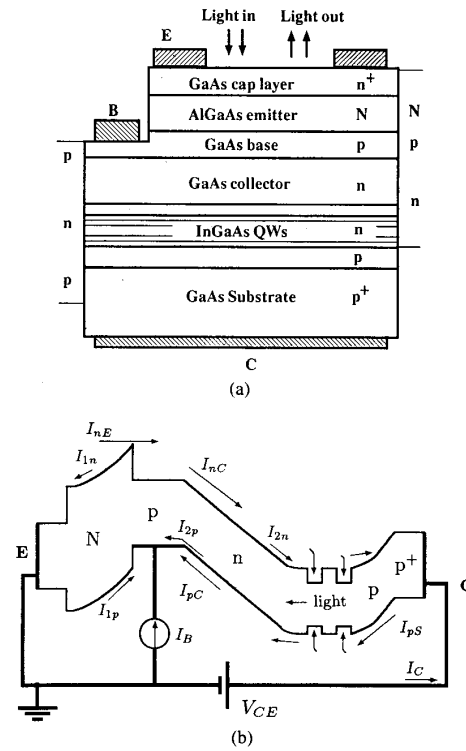


Fig. 1. Schematic layer structure (a) and the band diagram (b) of the investigated photothyristor structure biased in OFF state. Electron and hole current components are denoted by subscripts n and p , respectively.

bine in the quantum wells and the photoregenerated carriers in the depleted collector and neutral base of the N-p-n device create additional base current (I_{pC}) constituting a positive feedback mechanism. The emission energy of the LED's was intentionally chosen to be smaller than the GaAs bandgap to avoid an undesirably large feedback resulting from self-absorption generation in the N-p-n HBT. A small optical feedback allows the switching characteristics of the device to be controlled by the emitter-base junction bias of the N-p-n HBT. In the investigated device, the entire spectrum of the emitted light is at energies below the GaAs band edge (Fig. 3). Therefore, the optical feedback is negligible. If desired, a larger electrooptical feedback can be achieved by a different LED quantum well design.

For the three-terminal device, using the notation from Fig. 1(b), the current relations can be derived as follows [14]:

$$I_{nE} = I_{pS} + I_B \quad (1)$$

and

$$I_{pS} = I_{nC} + I_{pC} + I_{C0} \quad (2)$$

where I_{C0} is the saturation current. Common-base current gains α_N and α_P are defined as

$$I_{nC} = \alpha_N \cdot I_{nE} \quad \text{and} \quad I_{pC} = \alpha_P \cdot I_{pS} \quad (3)$$

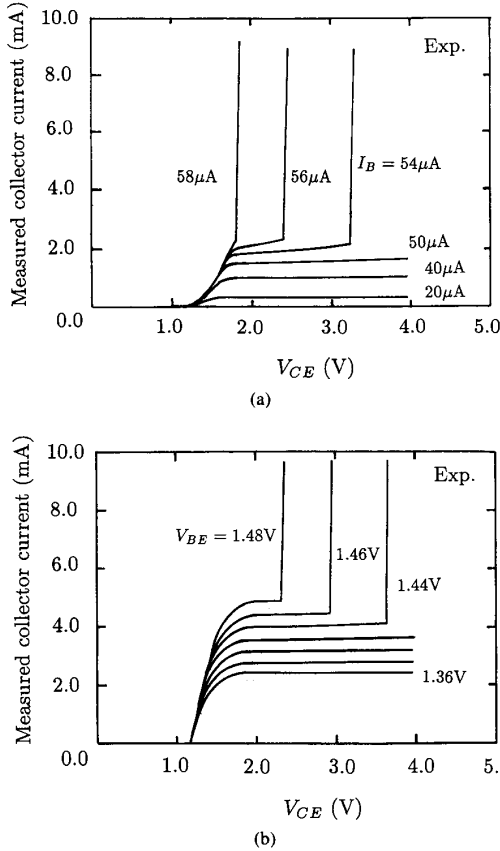


Fig. 2. Current-voltage characteristics of the HBT-LED (emitter size is $10 \times 40 \mu\text{m}^2$) for (a) constant base current steps and (b) constant base-emitter voltage steps.

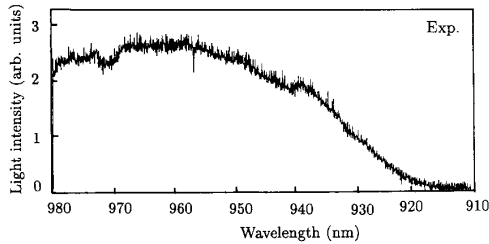


Fig. 3. Spectrum of light output from a $300 \mu\text{m}$ circular device in ON state (current = 200 mA).

From (1)–(3)

$$I_{pS} = \frac{\alpha_N I_B + I_{C0}}{1 - \alpha_N - \alpha_P}. \quad (4)$$

Note that I_{pS} is the measured collector current where the use of subscript p emphasizes that the hole current is supplied by the p^+ -substrate. This notation was chosen to avoid confusion with the other current components in the collector of the N-p-n HBT. As can be seen from (4), the switch ON condition is reached when $\alpha_N + \alpha_P = 1$. We

expect α_P to be quite small due to recombination in the InGaAs QW's, the relatively thick base region, the homojunction emitter, and the emitter-down configuration of the p-n-p transistor. The variation of the relatively smaller α_P is neglected in our model. Therefore, switching can be controlled by modulating α_N through the base bias.

In the N-p-n HBT, common-base current gain α_N is given as [15]

$$\alpha_N = \gamma_N \alpha_T M \quad (5)$$

where γ_N is the emitter efficiency, α_T is the base transport factor, and M is the collector multiplication factor. For ordinary collector-emitter voltage biases, $M \approx 1$; and for base widths much smaller than the diffusion length, $\alpha_T \approx 1$. The current gain is then almost entirely determined by the emitter efficiency under normal operating conditions, i.e., $\alpha_N \approx \gamma_N$ [15]. For the investigated structure, the base width is sufficiently small ($0.1 \mu\text{m}$) to justify this approximation. Moreover, when constant collector-base is considered, the base transport factor and collector multiplication factor remain unchanged at different injection levels.

The emitter efficiency of AlGaAs-GaAs HBT's (α_N for our device) increases with increasing base-emitter current density, as the contribution of the surface and bulk recombination currents becomes relatively small compared to the diffusion current across the base region [15]. Therefore, the feedback can be controlled by the external base bias or by optical excitation. Neglecting the recombination of the hole currents from the collector and the external base current in the neutral base, the total base-emitter hole current I_{BT} can be written as

$$I_{BT} = I_B + I_{pC} + I_{2p} - I_{1p} \quad (6)$$

where I_{1p} and I_{2p} are the hole currents due to photo-generated carriers in the N-AlGaAs emitter and in the GaAs p-n base-collector regions, respectively [Fig. 1(b)].

To determine the values of α_N and α_P at the switch ON point, we compare the I - V curves for constant base current [Fig. 2(a)] and constant base voltage [Fig. 2(b)]. The value of α_N is a function of the total base current ($I_B + I_{pC}$ in the absence of optical excitation) of the N-p-n HBT and we can expect that the instability condition occurs at a certain threshold value of $I_B + I_{pC}$. We will consider the transition at $V_{CE} = 3 \text{ V}$. From Fig. 2(a) and (2) we obtain $I_B \approx 54.5 \mu\text{A}$ and $I_{pC} = (\alpha_P \cdot I_{pS}) = 2.2 \cdot \alpha_P \text{ mA}$. Examining Fig. 2(b), we obtain $I_{pC} = 4.4 \cdot \alpha_P \text{ mA}$. In this case, I_B decreases as the switch ON condition is approached and is less than $5 \mu\text{A}$ at the switching threshold. Equating the total base currents for the constant base-emitter voltage and base current conditions

$$(0.0545 + 2.2\alpha_P) \text{ mA} = (0.005 + 4.4\alpha_P) \text{ mA}. \quad (7)$$

Solving (7) gives $\alpha_P = 0.023$. From $\alpha_N + \alpha_P = 1$ we deduce that $\alpha_N = 0.977$ which corresponds to a common emitter current gain of $h_{FE} = 42.5$. That is, at $V_{CE} =$

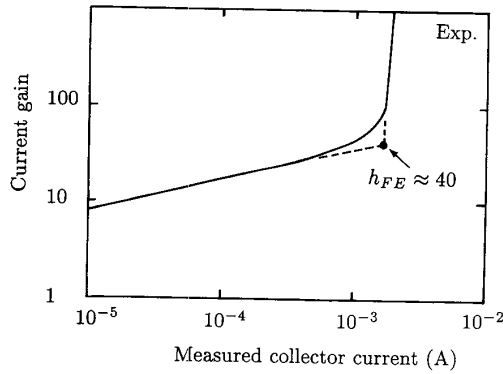


Fig. 4. Current gain versus collector current for a $10 \times 40 \mu\text{m}^2$ emitter device. Dashed line is the extrapolation of the gain curve from low current region.

3 V, switching occurs when the current gain of the N-p-n HBT exceeds 42.5.

This dependence of the switch ON condition on current gain can be experimentally confirmed by plotting current gain versus measured collector current (I_{pS}) as the base current is swept at $V_{CE} = 3$ V (Fig. 4). The curve for $h_{FE} - I_C$ is similar to the typical HBT characteristics at low current levels. The slope of $\log(h_{FE}) - \log(I_C)$ reflects a base-emitter ideality factor of 1.5 which is in good agreement with the measured value of 1.45. At higher current levels, due to the positive feedback, the current gain increases more rapidly than in conventional HBT's and switching takes place. Just before switching occurs, the component of the base current supplied by the feedback mechanism (I_{pC}) becomes comparable to the external base current component (I_B). Therefore, the apparent current gain when the feedback becomes substantial is $\alpha_N(1 + \alpha_p\alpha_N + \dots)$ which differs from the internal gain of the HBT. We estimate the actual current gain $h_{FE} = \alpha_N / (1 - \alpha_N)$ at the switching condition by extrapolating the gain curve from the low current regime as shown in Fig. 4. The current gain at the onset of switching obtained by this method is about 40, in very good agreement with the calculated $h_{FE} = 42.5$.

As a further verification of our picture of the switching behavior presented above, we compare the current density and current gain at the switch ON condition in devices with various emitter perimeter to area ratios. As can be seen in Fig. 5, the current density at which switching occurs varies from 200 A/cm^2 to nearly 800 A/cm^2 whereas the critical current gain is independent of the device geometry within the accuracy of our measurements.

Fig. 6 shows the Gummel plot of the investigated device. In this figure, the different switching conditions for constant base voltage and constant base current I_B can easily be identified. Note that the base and collector currents are monitored as the V_{BE} is swept. The sudden increase in the collector current (arrow 2) corresponds to the switching condition at a constant base voltage. Where I_B reaches its maximum (arrow 1) is the switching threshold at a constant base current. At this point the derivative of the col-

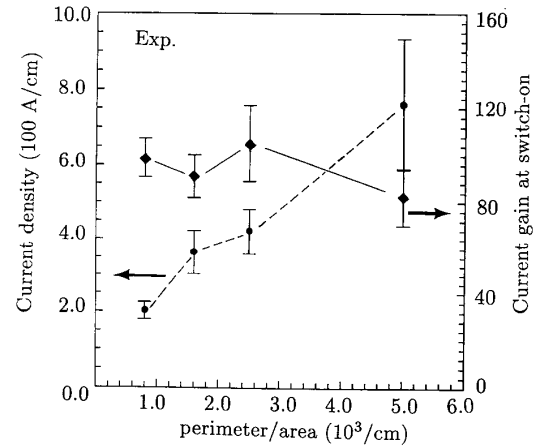


Fig. 5. Dependence of critical current density and current gain for switch ON versus perimeter to area ratio.

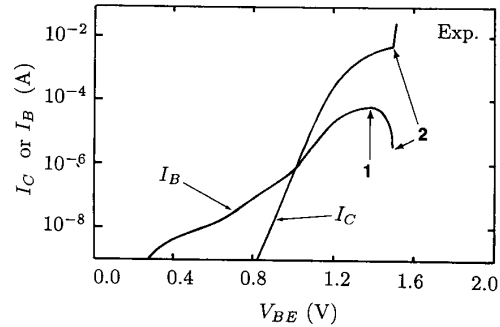


Fig. 6. Gummel plot for the investigated device. At point 1: $I_B = 55 \mu\text{A}$ and $I_C = 2.2 \text{ mA}$ and at 2: $I_B < 5 \mu\text{A}$ and $I_C = 4.4 \text{ mA}$.

lector current with respect to the base current is infinite. If the base current can be increased beyond this maximum value, the collector current will switch to high current ON state. As expected, these values for the switching conditions for constant current and constant voltage are in good agreement with the current levels observed in Fig. 2(a) and (b), respectively. We interpret the downturn in I_B to be due to the increasing effect of the parasitic resistances at high current levels which reduces the fraction of the externally supplied V_{BE} dropping across the emitter-base junction. As the switching point denoted by arrow 2, the base current is an order of magnitude smaller than its maximum, and after switching it settles to a value determined by the external circuitry.

In the above section, we have analyzed in detail the electrical properties of a three terminal N-p-n HBT-LED device including its switching behavior under different applied base bias conditions. It is possible to replace the electrical base bias with optical excitation. The N-p-n device then operates as a heterojunction phototransistor (HPT). In the following section, we explore the additional device functions when the device is operated in this manner.

IV. WAVELENGTH SELECTIVE OPTICAL SWITCHING

A. Two Wavelength ON-OFF Switching

As discussed earlier, photothyristor switching can be induced by modulating the total base current by means of optical excitation instead of biasing through an electrical contact. Examining (6) and Fig. 1, we deduce that I_{BT} can be increased if the carriers are photogenerated in the collector-base depletion region and a reduction in the total hole current results when photogeneration occurs in the emitter-base depletion region. We consider two distinct optical excitations, namely a He-Ne gas laser operating at $\lambda_1 = 6328 \text{ \AA}$ and a GaAs diode laser operating at $\lambda_2 \approx 8600 \text{ \AA}$. Under He-Ne laser (λ_1) excitation, most of the incident light is absorbed in the emitter due to the large absorption coefficient of AlGaAs at this wavelength ($I_{1p} \gg I_{2p}$) resulting in a reduction of I_{BT} [see (6)]. The AlGaAs emitter is transparent to the GaAs laser (λ_2), so in this case photogeneration occurs only in the GaAs base and collector ($I_{2p} \gg I_{1p}$) resulting in increased I_{BT} as given in (6). Therefore, optical excitations at different wavelengths (λ_1, λ_2) can be used to influence I_{BT} , modulating α_N , and causing the photothyristor to switch ON (λ_2) and OFF (λ_1), i.e., to function as a wavelength discriminating optical switch (WDOS).

Fig. 7 shows the I - V characteristics of the WDOS as V_{cc} is swept while the external base current is kept constant. The switch ON without the external circuit occurs at the point denoted by I_S and V_S , i.e., switching current and voltage, respectively. The complete circuit, which dictates the particular value of the ON state current level (I_h'), is pictured in the inset. When V_{cc} is swept down from the ON state, switch OFF occurs at I_h (the holding current) regardless of the external circuit configuration. The amount of hysteresis between the switch ON and switch OFF current levels is dictated by the external circuit. Lines 1, 2, and 3 highlight values of V_{cc} which enable different device functions of the WDOS. We emphasize that the position of these lines is determined by the applied V_{cc} while the slope is determined by the external resistor. Along the load line 1 (V_{cc1}), two stable conditions exist at its intercepts (A and B) with WDOS I - V characteristics. Fig. 8 schematically shows the change in the I - V characteristics of the WDOS under illumination by either λ_1 or λ_2 , while the inset gives the measured critical current levels (I_h, I_h') as a function of the base bias. Referring to Figs. 7 and 8, we see that when λ_2 is incident on the WDOS, the new I - V characteristics no longer intersect the load line at point A. The only stable condition is the intercept at point B, and the WDOS switches ON. Point B is common to both curves so that when λ_2 is removed, the WDOS remains in the ON state, illustrating the bistability of the WDOS at V_{cc1} . When λ_1 is incident, point B is no longer an intercept of the new I - V characteristics, and the device must switch to the OFF state.

Table I summarizes the experimentally observed output states of the WDOS in the form of a truth table which illustrates the logic functions. At V_{cc2} , the WDOS is an

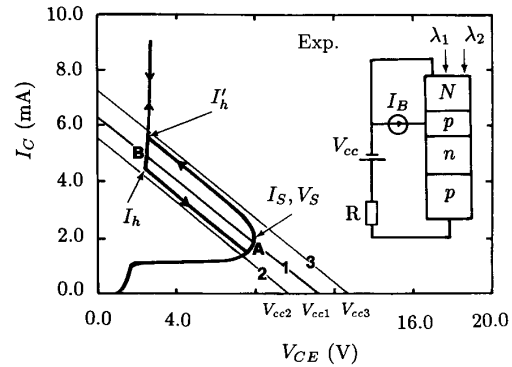


Fig. 7. Current-voltage characteristics of the WDOS (emitter size $10 \times 40 \mu\text{m}^2$) as the collector voltage is swept for $I_B = 40 \mu\text{A}$. The external circuit configuration is shown in the inset ($R = 1.8 \text{ k}\Omega$). Three interesting load lines obtained for different V_{cc} values are shown as 1, 2, and 3. The switch ON condition is denoted as I_S, V_S where derivative of the current is infinite.

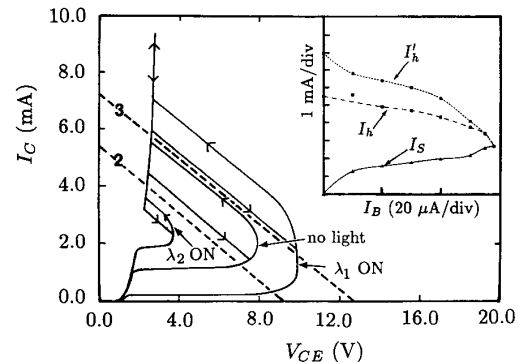


Fig. 8. Schematic I - V characteristics for the WDMOS showing the influence of λ_1 and λ_2 illumination. Dashed lines (2 and 3) show the load lines. Inset illustrates the actual measured critical current values as a function of I_B .

TABLE I
EXPERIMENTALLY DEMONSTRATED LOGIC FUNCTIONS OF THE WDOS.
INTENSITY OF THE OPTICAL EXCITATIONS ARE DENOTED WITH $I(\lambda_i)$ AND
COMPARISON IS QUALITATIVE. DIFFERENT LOADLINES DEPICTED IN FIG. 7
ARE SHOWN AS V_{cc2} AND V_{cc3}

INPUT		OUTPUT			
		$I(\lambda_1) > I(\lambda_2)$		$I(\lambda_1) < I(\lambda_2)$	
λ_1	λ_2	V_{cc2}	V_{cc3}	V_{cc2}	V_{cc3}
0	0	0	1	0	1
0	1	1	1	1	1
1	0	0	0	0	0
1	1	0	0	1	1
FUNCTION		$(\bar{\lambda}_1 \cdot \lambda_2)$	$\bar{\lambda}_1$	λ_2	$(\bar{\lambda}_1 + \lambda_2)$

AND gate for λ_2 and the inverted λ_1 or a noninverter for λ_2 . At V_{cc3} , the WDOS is either an inverter for the λ_1 input or an OR gate for the λ_2 and the inverted λ_1 inputs. In addition to these logic functions, when biased at V_{cc1} , the WDOS is bistable and can be used as a completely

optical read-write memory. Because of the different wavelengths of the GaAs laser, He-Ne laser and the QW LED, a single optical window is sufficient.

B. Multiple Wavelength Selective Switching

The two wavelength ON-OFF switching described above can be extended to multiple closely spaced wavelengths for switch ON by integrating the photothyristor into a resonant cavity. We first review the enhanced photosensitivity and wavelength selective detection properties of resonant cavity-enhanced (RCE) photodetectors and compare with experiments [16]–[18]. The wavelength selectivity and tunable narrow-band response of the RCE scheme is then combined with the optical switching characteristics of the photothyristor and a novel wavelength demultiplexing optical switch is demonstrated.

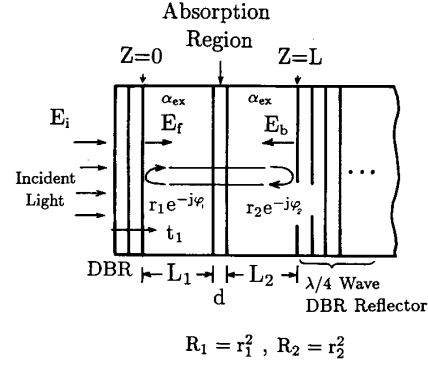
1) *Formulation of Photosensitivity for RCE Detection*: We first derive an expression for the quantum efficiency of RCE photodetectors using the illustration in Fig. 9. Both of the end mirrors of the RCE photodetector may be made of quarter wavelength stacks of semiconductor compounds or dielectric materials. For the top mirror, the native semiconductor to air interface can also be utilized, providing a reflectivity of approximately 30%, owing to the large refractive index difference at the boundary. The active layer, of thickness d and absorption coefficient α , where the photogeneration of carriers takes place, lies in the optical cavity between the two mirrors. Distances from the top and the bottom mirrors to the active layer are denoted by L_1 and L_2 , respectively. The field reflection coefficients of the top and the bottom mirrors are $r_1 e^{-j\psi_1}$ and $r_2 e^{-j\psi_2}$, respectively, where ψ_1 and ψ_2 represent phase shifts caused by the penetration of the light into the multiple-layer mirror region. The corresponding power reflectivity is $R_i = r_i^2$ ($i = 1, 2$).

The electric field component E_i of an incident light-wave is transmitted into the detector as $t_1 \cdot E_i$. In the detector region the forward traveling field E_f is composed of this transmitted field and the field which is reflected from the bottom mirror. By self-consistently calculating the electric field and power density within the cavity, the quantum efficiency η can be shown to be [16]:

$$\eta = \left\{ \frac{(1 + R_2 e^{-\alpha d})}{1 - 2\sqrt{R_1 R_2} e^{-\alpha d} \cos(2\beta L + \psi_1 + \psi_2) + R_1 R_2 e^{-2\alpha d}} \right\} \times (1 - R_1)(1 - e^{-\alpha d}) \quad (8)$$

where $\beta = 2n\pi/\lambda$ (λ : wavelength and n : refractive index).

The quantum efficiency η is a periodic function of the inverse wavelength as illustrated in Fig. 10. Three curves are drawn for $R_1 = 0.9, 0.3,$ and 0.05 assuming $R_2 = 0.9, \alpha d = 0.1,$ and $L = 2 \mu\text{m}$. The quantum efficiency is enhanced periodically at resonant wavelengths determined by $2\beta L + \psi_1 + \psi_2 = 2m\pi$ ($m = 1, 2, 3 \dots$). On the right-hand side of (8), the term inside the brackets gives the cavity enhancement effect. This term becomes unity when $R_2 = 0$ giving the quantum efficiency for a conventional detector without the cavity structure, i.e., η



$$R_1 = r_1^2, R_2 = r_2^2$$

Fig. 9. Analysis model of resonant cavity enhanced (RCE) photodetectors.

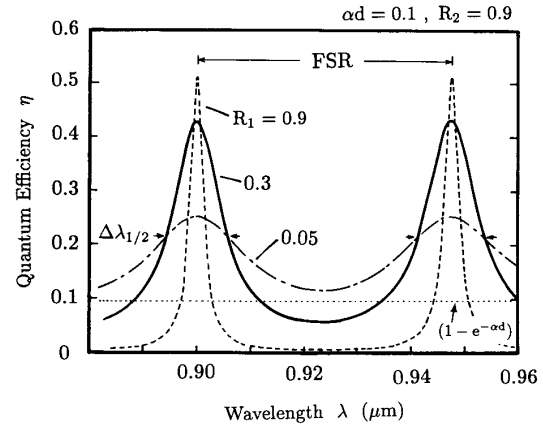


Fig. 10. Wavelength dependency of the quantum efficiency for RCE detectors for various top mirror reflectivities $R_1 = 0.05, 0.3,$ and $0.9,$ respectively, at absorption parameter $\alpha d = 0.1,$ and the bottom mirror reflectivity $R_2 = 0.9.$

$= (1 - R_1)(1 - e^{-\alpha d})$. The dotted line in Fig. 10 indicates the value given by $1 - e^{-\alpha d}$, the maximum η value attainable for a conventional photodetector.

At the off-resonance points, i.e., $2\beta L + \psi_1 + \psi_2 = (2m + 1)\pi$ ($m = 1, 2, 3 \dots$), the field amplitude of the light between the two end mirrors decreases due to de-

structive interference of the forward and backward traveling waves and the quantum efficiency is suppressed as shown in Fig. 10. The wavelength spacing between neighboring resonant peaks, i.e., the free spectral range (FSR), is:

$$\text{FSR} = \frac{\lambda^2}{2n(L + L_{\text{eff},1} + L_{\text{eff},2})} \quad (9)$$

where $L_{\text{eff},i}$ are the effective optical length of the multiple-layer mirrors. The ratio of the FSR to the wavelength full

width at half maximum $\Delta\lambda_{1/2}$ is a measure of the wavelength selectivity of detection. This ratio is usually referred to as the finesse F , and can be derived from (8) as follows:

$$F = \frac{\text{FSR}}{\Delta\lambda_{1/2}} = \frac{\pi(R_1R_2)^{1/4}e^{-\alpha d/2}}{1 - \sqrt{R_1R_2}e^{-\alpha d}}. \quad (11)$$

Fig. 10 clearly shows the increase of F with increasing top mirror reflectivity as a result of the narrowing $\Delta\lambda_{1/2}$. A large top mirror reflectivity is desirable for highly wavelength selective detector response.

Generally, $L_{\text{eff},i}$ can be given by:

$$L_{\text{eff},i} = \frac{1}{2} \frac{\partial\psi_i}{\partial\beta} \quad (i = 1, 2). \quad (10)$$

A typical L_{eff} value for a pair of GaAs–AlGaAs stacked layer mirrors (top : five periods, bottom : eight and one half periods) is $0.7 \mu\text{m}$ [19].

For very thin active layers ($d \ll \lambda/2n$), the field distribution inside the cavity becomes important. For instance, if the active layer is situated near a minimum, the optical response will be poor, whereas if the active layer is in the vicinity of a standing wave maximum, the optical response of the device will be enhanced. The influence of the standing wave effect on the photosensitivity can be formulated in terms of an effective absorption coefficient α_{eff} which replaces α in all of the equations. The dependence of the α_{eff} on the cavity parameters (Fig. 9) is given as [20]:

$$\alpha_{\text{eff}} = \alpha \left\{ 1 + \frac{2r_2}{\beta d(1+r_2^2)} \cdot [\sin \beta d \cos (2\beta L_2 + \beta d + \psi_2)] \right\}. \quad (12)$$

Note that, when $d = \lambda/2n$, the absorbing region overlaps one period of the standing wave and the standing wave effect becomes unity. In our experimental devices, the absorbing layer thickness ($d = 0.1 \mu\text{m}$) was approximately equal to $\lambda/2n$ ($\approx 0.125 \mu\text{m}$ at $\lambda = 0.9 \mu\text{m}$). For simplicity, we will not consider the standing wave effect in the remaining discussion, although it can easily be included [20].

2) *Wavelength Demultiplexing AlGaAs–GaAs Heterojunction Phototransistors*: RCE detection can be realized for AlGaAs–GaAs HPT's through the use of an intermediate smaller band-gap (InGaAs) collector layer [17]. Fig. 11 shows the structure of an AlGaAs–GaAs RCE-HPT where the resonant cavity is formed between the embedded quarter wavelength stack AlAs–GaAs bottom mirror ($R_2 = 0.9$) and the epitaxial layer surface. By introducing the InGaAs layer, the photosensitivity spectrum extends to longer wavelengths ($> 900 \text{ nm}$) where the absorption in the base and the heavily doped GaAs collector is negligible. Having a lossless structure, except for the thin active region, enables the formation of a high quality factor Q cavity. The estimated Q of the cavity for the lossless

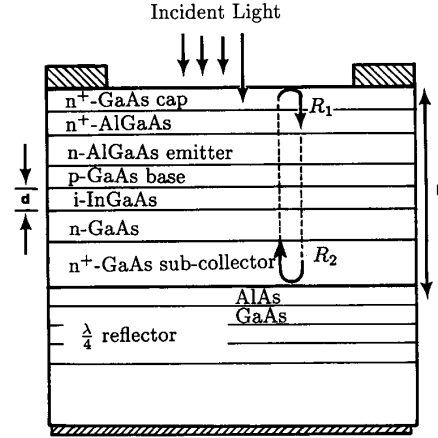


Fig. 11. Schematic layer structure of the investigated RCE-HPT's.

case is about 75 at $\lambda = 900 \text{ nm}$. The measured Q with a $0.1 \mu\text{m}$ InGaAs absorbing layer is 60 which is only a 20% reduction from the value for the lossless cavity case.

The photosensitivity spectrum of the RCE-HPT is shown in Fig. 12 (dashed line) along with that of the conventional HPT without a mirror (solid line) for comparison. The spectral response of the conventional HPT decreases sharply around the band edge wavelength of GaAs at 860 nm , with a small increase at around 900 nm which is due solely to absorption in the InGaAs layer. Under pulsed laser illumination, the optical gain of the HPT is measured to be above 500 at 850 nm (calculated $\eta = 25\%$) and 150 at 900 nm (InGaAs region absorption wavelength, $\eta = 6.7\%$) at $V_{ce} = 5 \text{ V}$ and $I_c = 30 \text{ mA}$ [21]. The photosensitivity of the RCE-HPT is greatly enhanced at certain wavelengths, as shown in Fig. 12. At the resonant peak of 900 nm , where the low loss cavity is attained, the detected current increases to 7 times that of the HPT without reflectors. This resonant cavity enhancement coincides closely with the calculated enhancement factor of 6.5 for the same reflectivities and active layer thickness. Wavelength selectivity is demonstrated through the low responsivity of the RCE-HPT to off-resonance wavelengths which are rejected by the optical cavity.

We can construct a wavelength demultiplexer consisting of several RCE-HPT's which are tuned to different resonant wavelengths by varying the total optical cavity length of each device [19]. This can be achieved by recessing the epitaxial layer surface by, for example, conventional wet chemical etching. Such a demultiplexing detector was realized (Fig. 13) by recessing the surface of adjacent detectors by 350 , 700 , and 1050 \AA to obtain three equally spaced resonant modes thereby maximizing the crosstalk attenuation. The four RCE-HPT's provide complementary optical responses determined by the total optical length of the cavity ($2\beta L + \psi_1 + \psi_2$). Each device functions as a channel discriminator detecting a narrow band of light from the incident light beam common to all of the detectors. Although the detected photocurrent of

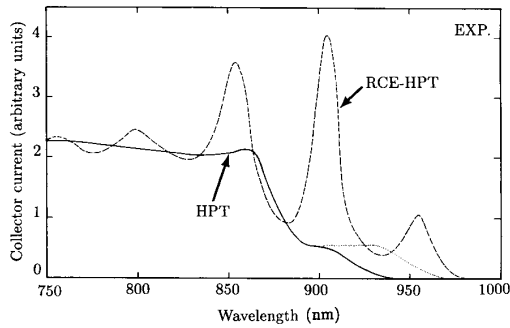


Fig. 12. Spectral response of floating base HPT's, (i) without reflectors (solid line) and (ii) with resonant cavity enhancement (dashed line). The dotted line shows the estimated spectrum for the latter when the cavity influence is removed. Note that, the band edge of the InGaAs region moves to longer wavelengths due to inaccuracy in the In mole fraction.

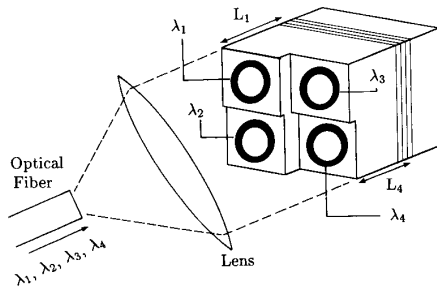


Fig. 13. Conceptual diagram of an application for the demultiplexing detector composed of four RCE-HPT's with different resonance wavelengths.

each individual detector is decreased due to the sharing of the incident power, the larger RCE gain more than compensates. This scheme provides a simple but effective wavelength demultiplexing detection scheme which is especially suited for small channel number demultiplexing or short distance wavelength division multiplexing (WDM) [22] communication systems.

Fig. 14 shows the spectral responses of devices #1-3 under equal illumination and a collector emitter bias of 3 V. The FSR of the device was around 55 nm at 900 nm center wavelength and the $\Delta\lambda_{1/2}$ was 15 nm resulting in a finesse $F = 3.6$. The maximum crosstalk attenuation for dual wavelength demultiplexing was demonstrated to be over 6:1 (15 dB). For three wavelength demultiplexing, the crosstalk attenuation is around 4:1 (12 dB), slightly below the theoretical value of 15.6 dB for $F = 3.6$ and $N = 3$ [21].

Using the wavelength dependent quantum efficiency equation (8) for RCE detectors, the interchannel crosstalk attenuation (C) can be derived approximately as a function of finesse and number of channels (N) as [16]:

$$C \approx 20 \log \left[1 + \left(\frac{2F}{N} \right)^2 \right] \quad (N > 3) \quad (13)$$

where the finesse is given by (12). From (13), we note that low crosstalk can be obtained for a very high finesse

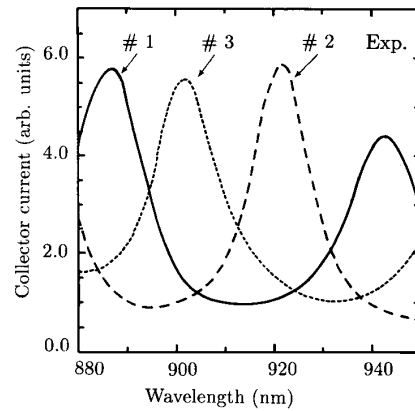


Fig. 14. Spectral response of the three devices with different surface recessing depicted in Fig. 12. The portion of the wavelength spectrum over one free spectral range with minimum crosstalk is shown.

cavity formed by increasing the end mirror reflectivities while maintaining a thin absorption layer. For example, when $\alpha d = 0.01$, $F = 100$ can be expected for end mirror reflectivities of $R_2 = 0.99$ and $R_1 = 0.985$. It is possible to optimize the device structure with the crosstalk and quantum efficiency in mind. Taking an absorbing layer thickness of $0.1 \mu\text{m}$ (i.e., $\alpha d = 0.1$), the dependencies of both C and η on the mirror reflectivities are plotted in Fig. 15.

In the above prototype device, the buried mirror is only ten periods with a corresponding peak reflectivity of $R_2 = 90\%$ and the top mirror is the epilayer surface with $R_1 = 30\%$. Increasing the number of periods for the bottom mirror to 15 will result in 99% peak reflectivity and enhance the wavelength selectivity leading to a drastic improvement of the demultiplexing performance. For example, when $R_1 = 0.90$, $R_2 = 0.99$, and $\alpha d = 0.1$, F is 20, resulting in crosstalk attenuation values of 24 and 40 dB for 10 and 4 channel demultiplexing, respectively, while η is 85%.

3) *Wavelength Demultiplexing Optical Switch*: When the concepts of the WDOS and resonant cavity enhancement are combined, the result is a wavelength demultiplexing optical switch (WDM-OS) which is most easily understood as an RCE-HPT which drives a QW-LED. The layer structure of the WDM-OS device is very similar to the photothyristor shown in Fig. 1. The photothyristor structure for the WDM-OS is grown on an AlAs-GaAs mirror forming a resonant cavity with the native GaAs surface as depicted in Fig. 11. The HPT has a composite collector consisting of $\text{In}_{0.08}\text{Ga}_{0.92}\text{As}$ and GaAs regions. The wavelength spectrum of the HPT photosensitivity at low excitation power is shown in Fig. 16 for an as-grown device (solid line). The dashed line illustrates the shift in the resonant wavelengths of the cavity which is obtained when the top surface is recessed by wet chemical etching. For a given cavity length, the sensitivity is enhanced by resonance while the incident light is rejected at off-resonance wavelengths [16], [21] providing wavelength selec-

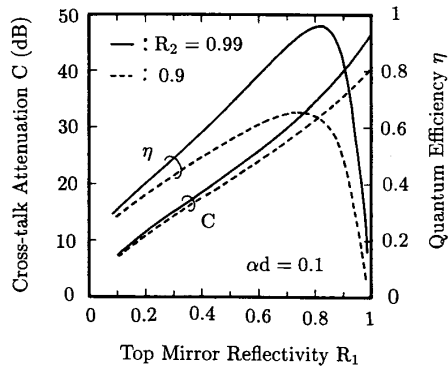


Fig. 15. Crosstalk attenuation and quantum efficiency of the investigated wavelength demultiplexing detector as a function of the top mirror reflectivity. The solid line shows η and C for $R_2 = 0.99$ and the dashed line for $R_2 = 0.9$.

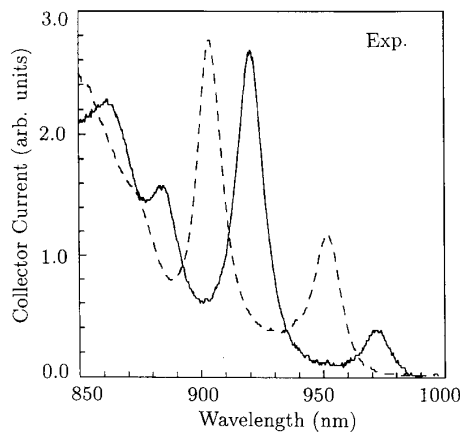


Fig. 16. Spectral response of the WDM-OS under monochromatic light for the as-grown structure (solid line) and after surface is recessed (dashed line).

tivity. By changing the cavity length, the resonant wavelengths can be tuned within the range provided by the InGaAs absorption region and the AlAs–GaAs mirror. This scheme allows devices with complementary photosensitivities to be easily fabricated on the same wafer in any arbitrary pattern.

In the structure described above, the vertical integration of the RCE-HPT with the InGaAs–GaAs LED allows the HPT to drive the LED in an N–p–n–p configuration. The resulting device is a switch having a wavelength selective response to optical stimuli. The common-emitter current-voltage (I – V) characteristics of the WDM-OS are given in Fig. 17 for constant base current (I_B) steps. The inset shows the dependence of the collector current on the base current at constant collector-emitter voltage (V_{CE}). Note that in the absence of base current, the breakdown occurs for $V_{CE} > 16$ V. A dark current of 6×10^{-6} A/cm² and $< 10^{-4}$ A/cm² at $V_{CE} = 5$ V and $V_{CE} = 15$ V, respectively, was measured in devices fabricated without a base contact.

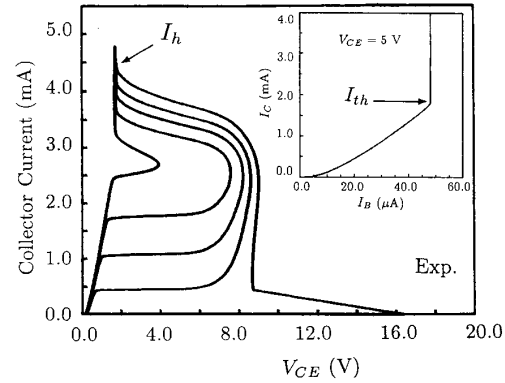


Fig. 17. Current–voltage characteristics of the WDM-OS (emitter size $50 \times 50 \mu\text{m}^2$) as base current is stepped. The inset shows the measured dependence of the collector current on the base current at constant collector emitter bias ($V_{CE} = 5$ V).

As can be seen from the inset in Fig. 17, the collector current (I_C) increases almost linearly with the base current until a threshold is reached. The base current can be applied either electrically through the base contact or optically from carrier generation in the InGaAs collector region. At the threshold, the collector current switches to a value limited only by the external circuit. The intensity of the optical excitation can be adjusted with regards to the switching threshold so that switching is only induced by excitation at the resonant wavelength. A large enhancement of the WDM-OS collector current at the resonant wavelength is then obtained as the device switches to the high current ON state.

Fig. 18 shows the evolution of the wavelength dependence of the collector current as the input excitation intensity is increased. The response is computed using the measured photosensitivity (Fig. 16) and I_C – I_B dependence (Fig. 17 inset) of the WDM-OS for a $50 \times 50 \mu\text{m}^2$ emitter size device. The excitation was assumed to have a constant photon flux across the spectral range corresponding to approximately $90 \mu\text{W}$ [Fig. 18(a)] and $170 \mu\text{W}$ [Fig. 18(b)] at the $1 \mu\text{m}$ wavelength. The resonant peaks of Fig. 18(a) have larger peak to valley ratios compared with Fig. 16 as a result of the non-linear dependence of the collector current on the base current (Fig. 17 inset). If the resonant optical input intensity creates a base current sufficient to surpass the WDM-OS switching threshold, a drastic increase in the amount of collector current at the resonant wavelengths is achieved [Fig. 18(b)]. The increase in the collector current due to the RCE effect leads directly to higher peak to valley ratios and lower crosstalk of the electrical–optical response of the neighboring devices.

In the investigated structure, the number of available channels is limited by the finesse of the resonant cavity. The cavity formed by using the GaAs surface as the top mirror offers a FWHM of 15 nm and the finesse is limited to less than 4 for practical cavity lengths [21]. A significant improvement in the wavelength selectivity can be ob-

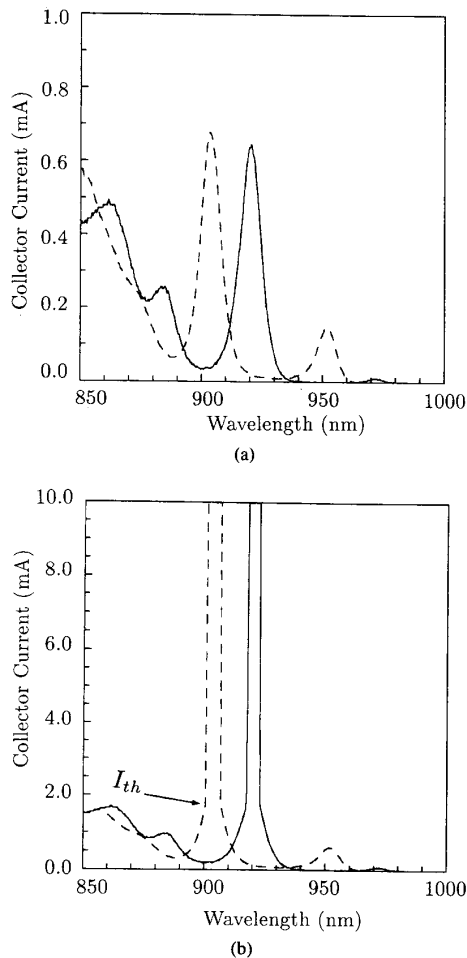


Fig. 18. Calculated spectral response of the WDM-OS for constant input photon fluxes corresponding to (a) $90 \mu\text{W}/\text{cm}^2$ and (b) $170 \mu\text{W}/\text{cm}^2$ at $1 \mu\text{m}$ wavelength. The experimental electrical characteristics and the optical response of the device have been taken as the bases of this calculated output. Note that, the current level after switching is set by the external circuit.

tained by increasing the top mirror reflectivity [16]. A FWHM of 3 nm was demonstrated for an HPT integrated in a resonant cavity formed with two periodic reflectors [23]. For such a high finesse structure it should be possible to obtain at least 10 channels within the accessible spectrum of the strained InGaAs-GaAs system. Realization of high finesse cavities tuned at multiple resonant wavelengths require a top mirror regrowth following the episurface recess. A dielectric stack can be used as the top mirror instead of a semiconductor stack to eliminate a second MBE growth. Recently, we have demonstrated a high finesse RCE structure utilizing a semitransparent metal film as the top reflector [24]. A finesse of 13.6, representing a 3.5 fold improvement, was realized.

We propose this novel wavelength selective optical switching device as input elements of the wavelength selective optical logic circuits. In the demonstrated device configuration of the WDM-OS, the QW-LED is employed

to generate a wideband optical output resulting in all optical switching. For cascadable wavelength selective operation, a narrow-band output source is essential. In the following section we discuss a fabrication technique towards the realization of multiple wavelength surface emitting laser arrays as alternative output devices. Using a separate device for the light output removes the need for the QW-LED within the WDM-OS. Elimination of QW's should increase the electrical feedback in the n-p-n-p structure resulting in a higher overall gain and sensitivity.

V. MULTIPLE WAVELENGTH SURFACE-EMITTING LASER ARRAYS

Due to their high packing density and ease of fabrication, vertical cavity surface emitting lasers (VCSEL) are very attractive sources for two dimensional (2-D) laser arrays [25], [26]. Such 2-D arrays emitting across a variable wavelength range are highly desirable for WDM applications, a key technology for increasing the transmission capacity of communication systems [22]. The key to developing multiple wavelength VCSEL arrays is to control the resonant modes of the optical cavity. Chang-Hasnain *et al.* [25] demonstrated a multiple wavelength 2-D VCSEL array which was obtained by varying the epitaxial thicknesses across the wafer during MBE growth. A wavelength span of 430 \AA with a small wavelength separation of 3 \AA was achieved from one end of the wafer to the other. However, any growth oriented technique for multiple wavelength VCSEL arrays will be limited by the strict dependence of the laser emission wavelengths on the relative position of the laser on the wafer.

We expect the surface recessing fabrication technique which we have demonstrated for RCE-HPT's and WDM-OS's to provide a significant improvement in the performance and flexibility of multiple wavelength VCSEL arrays over the scheme used in [25]. In this section, we describe how arbitrary arrangement of VCSEL's spanning a broad range of lasing wavelengths can be realized. The fundamental limitations of this scheme are theoretically investigated for AlAs-GaAs VCSEL's with strained InGaAs active regions operating at wavelengths near $\lambda = 1 \mu\text{m}$.

The schematic layer structure of the proposed VCSEL is shown in Fig. 19. The bottom mirror, with a reflection coefficient of $r_2 e^{-j\nu_2}$, is an M_2 period AlAs-GaAs quarter wavelength stack grown on a doped GaAs substrate. The top mirror is a hybridized design composed of a quarter wavelength stack (M_1) and a high reflectivity metal separated by a phase matching layer which has a reflection coefficient ($r_1 e^{-j\nu_1}$). The initial thickness of the GaAs spacer between the quarter wavelength stack and the metal is chosen as $3\lambda/4$ ($\approx 2200 \text{ \AA}$) to allow the maximum tuning range to be realized. The active region is placed in the middle of a GaAs layer of thickness $L = \lambda$ between the mirrors. In our calculations, we assume a $100 \mu\text{m}$ thick polished substrate with a quarter wavelength SiO_2 anti-reflection coating at the output window of the laser.

Fig. 20 shows the magnitude ($R_1 = |r_1|^2$) and the phase

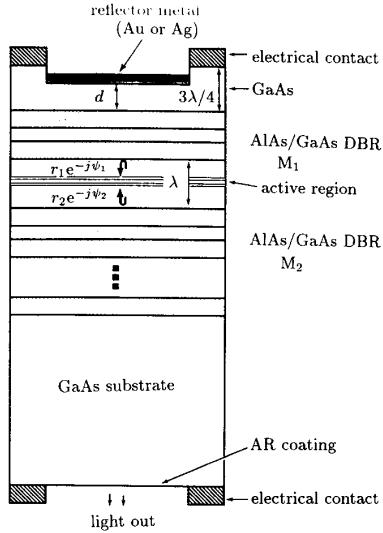


Fig. 19. Schematic layer structure of the proposed vertical cavity surface emitting lasers with hybrid top mirror. The reflector metal is deposited after the episurface is recessed to desired spacer thickness d which determines the reflectivity phase and thus the emission wavelength.

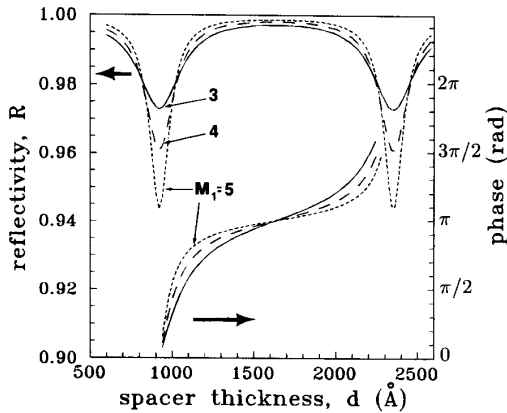


Fig. 20. The magnitude and phase of the reflectivity of the top mirror (R_1) as a function of the spacer thickness d for Ag metallization with various number of mirror periods (M_1).

(ψ_1) of the reflectivity for hybrid mirrors composed of a Ag metal reflector and various periods of the AlAs–GaAs mirror as a function of the spacer thickness d . Note that, the magnitude of the reflection coefficient remains nearly constant whereas the phase varies almost linearly within a considerable range of the spacer thicknesses. Although the metal–semiconductor interface alone forms a mirror with reasonable reflectivity, the additional quarter wavelength stack provides a significant improvement. For example, a Au–GaAs interface is $\approx 95\%$ reflective while Ag provides a reflectivity of $\approx 99\%$ in the 0.9 to 1.0 μm wavelength range [27]. Using the hybrid mirror structure with a 5 period AlAs–GaAs quarter wavelength stack, the total reflectivities will improve to 99.1 and 99.9%, respectively. Also, a larger phase variation is possible using

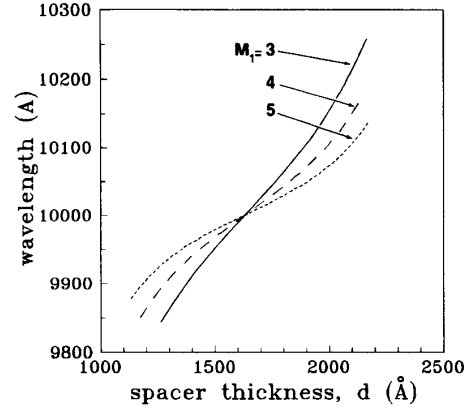


Fig. 21. The resonant wavelength dependence on the spacer thickness d for a cavity formed by a top hybrid mirror composed of M_1 (3, 4, or 5) periods of GaAs–AlAs quarter wavelength stack with Ag reflector and a $M_2 = 16$ periods of bottom quarter wavelength stack. The curves are plotted for a range of d where $(1 - R_2) > 2 \times (1 - R_1)$, and cavity finesse is larger than 400.

Ag instead of Au, as a result of Ag having a smaller real permittivity component.

The resonant condition of the VCSEL (Fig. 19) cavity is:

$$\begin{aligned} 2\beta L + \psi_2(\lambda) + \psi_1(\lambda, d) \\ = 2\beta(L + L_{\text{eff},2} + L_{\text{eff},1}) = 2m\pi \\ m = 1, 2, 3, \dots \end{aligned} \quad (14)$$

By means of recessing the episurface prior to the metal deposition, i.e., changing d , the phase of the top hybrid mirror, ψ_1 can be altered enabling a controlled variation of lasing wavelengths. One important limitation of the tuning range is the decreasing reflectivity (R_1) of the top mirror. For a structure with light output from the substrate side, the top mirror must remain more reflective than the bottom one. Throughout the entire available tuning range of the VCSEL considered here, we estimated that at least 2/3 of the light will be emitted through the bottom window, i.e., $(1 - R_2) > 2 \times (1 - R_1)$. Laser operation also depends critically on attainment of a high finesse cavity. Fig. 21 shows the dependence of the operating wavelength on the spacer thickness d for a VCSEL with a 16 period bottom mirror and a composite top mirror with Ag metallization and several different numbers of mirror periods. A continuous wavelength variation in excess of 400 \AA (4% at $\lambda = 1 \mu\text{m}$ which is well within the maximum demonstrated gain bandwidth of 10% for QW lasers [28]) is possible while the overall finesse of the optical cavity is maintained within 400 to 600. If Ag is replaced with Au, then a finesse in excess of 200 can still be maintained with a wavelength tunability of $\approx 120 \text{\AA}$ for $M_1 = 6$ and $M_2 = 14$.

The above method for fabricating multiple wavelength VCSEL arrays allows individual devices at arbitrary positions across the wafer to lase at a wavelength which is fixed during the fabrication process. Since the layer struc-

ture is identical throughout the wafer, any desired spatial distribution of emission wavelengths are possible which is a significant improvement over the alternative methods for multiple wavelength VCSEL's. This structure is superior to the LED outputs which were used for the WDOS and WDM-OS devices described above because the monochromatic VCSEL output is available as an input signal for a next level of optical logic. The output wavelength can be set during the fabrication process independent from the input wavelengths. Therefore, if the WDM-OS structure can be integrated with multiple wavelength VCSEL arrays, a cascadable completely optical logic unit can be realized. In the next section we propose the layer structure and fabrication layout of this combination and envision some of the optical logic functions which can be realized.

VI. MULTIPLE WAVELENGTH OPTICAL LOGIC GATES

In the previous sections we discussed the concepts for optoelectronic switches that can be turned on by multiple wavelength narrow band optical stimuli. We have also proposed a method, based on similar concepts, which enables the fabrication of 2-D VCSEL arrays capable of multiple wavelength lasing across a large wavelength range. Fig. 22 shows a design which monolithically integrates a WDM-OS and a VCSEL in a vertical fashion. The VCSEL is fabricated as described before by completely removing the layers constituting the WDM-OS. The optical cavity of the WDM-OS is complicated by the addition of the second quarter wave stack forming part of the VCSEL top mirror, but the new layers can easily be incorporated into the equations for the mirror reflectivity in the design of the WDM-OS. A similar structure consisting of a monolithically integrated photothyristor detecting a broadband optical input and driving a VCSEL has been demonstrated experimentally [11]. When the device pictured in Fig. 22 is fabricated, it will be capable of detecting a specific wavelength of light within any band accessible to the WDM-OS and emitting light within the tunability range of the VCSEL design. The result will be a wavelength selective optical logic (WSOL) circuit element capable of operation within any of a number of narrow bands which are chosen during the fabrication.

The WSOL device is very well suited for optical interconnect applications. By providing multiple channels, the number of optical fibers necessary to couple information in and out of an interconnect chip will be reduced by a factor equal to the number of wavelength channels accessible to the WSOL. The low crosstalk of the WSOL devices enables a closely packed multiple wavelength array to be fabricated whose light is coupled in and out of a single optical fiber. Such a configuration reduces the total number of optical fibers which must be coupled in and out of the interconnect chip, thereby greatly reducing the complexity and increasing the reliability of optoelectronic signal conversion.

Various logic operations can easily be performed with the WSOL circuit element by selecting appropriate input

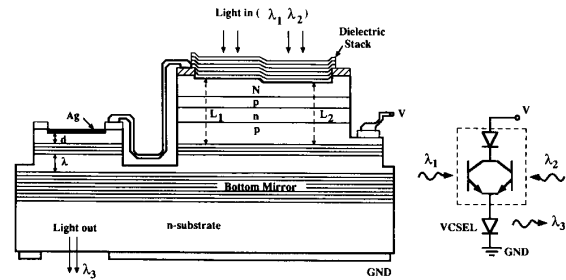


Fig. 22. Schematic representation of a wavelength selective optical OR gate. The input and output wavelengths are determined by setting L_1 , L_2 , and d during the fabrication.

and output wavelengths and forming the suitable electrical connections during the fabrication process. For example, Fig. 22 shows how the WSOL can be fabricated as an optical OR gate designed to respond to two different wavelengths and generate a third one. The input and output wavelengths are determined by setting the adjustable parameters L_1 , L_2 , and d . A top mirror for the detectors can be deposited after the completion of the fabrication to increase the input wavelength selectivity if more than three wavelengths is desired. Similarly, an AND gate can be realized in the manner depicted in Fig. 23. More complicated gate structures having several inputs and outputs at different wavelengths capable of performing higher level logic operations can be obtained by following the basic concepts depicted in Figs. 22 and 23. For instance, an XOR gate can be implemented in a six mesa structure illustrated schematically in Fig. 24. The XOR gate requires only a single optical fiber to couple light to the entire structure since the different inputs are discriminated through the wavelength selectivity of each WSOL device. The XOR output wavelength is also completely flexible within the tunability range of the VCSEL. This structure brings about a considerable simplification to a previously described two level single wavelength optical input-output XOR gate requiring nine mesas at each level [1].

Attributes of the WSOL device may be best exploited when circuits are designed to perform changing logic operations dependent on the set of incident wavelengths. If the XOR gate ($\lambda_1 \oplus \lambda_2$) described in the previous paragraph (Fig. 24) were modified so that WDM-OS #2 responds to two wavelengths λ_2 and λ_3 (as illustrated in Fig. 22), the XOR function remains unchanged if λ_3 is not incident. However, if only λ_1 and λ_3 are used, then the resulting logic function is that of an OR gate ($\lambda_1 + \lambda_3$). If all three wavelengths are used, then the overall function is $\lambda_1 \cdot \bar{\lambda}_2 + \bar{\lambda}_1 \cdot \lambda_2 + \bar{\lambda}_1 \cdot \lambda_3$. As the previous example, shows, the WSOL device can be used to construct reconfigurable circuits whose logical function can be changed by altering the set of input parameters

Another important aspect of the WSOL device is its cascability which allows performing sequential logic operations by placing a number of wafers in series. With present fabrication techniques a number of different wafers can be aligned so that the output signals from one

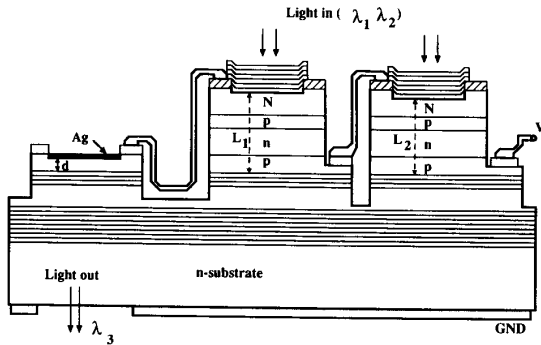


Fig. 23. Schematic representation of a wavelength selective optical AND gate. The input and output wavelengths are determined by setting L_1 , L_2 , and d during the fabrication.

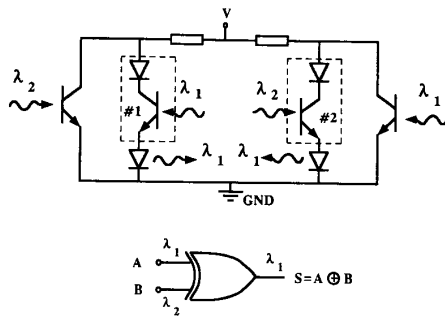


Fig. 24. Circuit representation of an XOR gate composed of WSOL devices sensitive to the indicated wavelengths. The XOR gate can be realized with six mesas.

wafer are used as the inputs of the next wafer. The low crosstalk resulting from the wavelength selective operation of WSOL relaxes the requirements for accurate alignment between the wafers forming the different levels. Rather, the problem now becomes ensuring that the output of a single VCSEL illuminates the entire array of WSOL elements constituting the next logic stage. A simple calculation [29] of the divergence of Gaussian VCSEL beams having initial radii of $10 \mu\text{m}$ and $6 \mu\text{m}$ yields respective spot sizes of $\approx 130 \mu\text{m}$ and $210 \mu\text{m}$ at a distance of $1000 \mu\text{m}$. The inherent divergence of the VCSEL output beam is detrimental for single wavelength systems where crosstalk is critical. Either devices must be widely spaced or routing from the specific outputs to the desired input coordinates is required. On the other hand, for wavelength selective logic gate arrays, the divergence eliminates the need for any physical interconnections since each optical outputs can be made to illuminate all the inputs at the next level [as illustrated in Fig. 25(a)].

As an example of the benefits of cascable operation, we have designed a FULL ADDER composed of two wafers containing 11 mesas each as shown in Fig. 25(a) and (b). The two levels are made identical except for a single change in the internal electrical connections so that the processing of each level can occur simultaneously. Al-

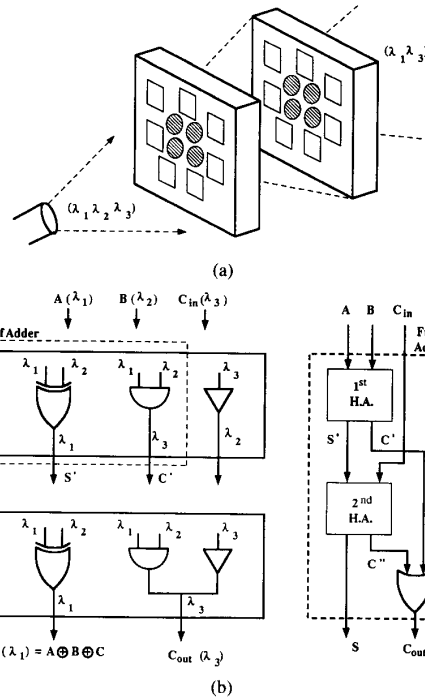


Fig. 25. The conceptual diagram showing the FULL ADDER which can be implemented using the WSOL devices. The two levels of wafers (a) forming the FULL ADDER and the gate representation with the corresponding input/output wavelengths (b) are illustrated.

though the same set of wavelengths are used as inputs and outputs, we do not expect any interference between levels since the high reflectivity bottom mirror in each wafer will prevent stray input light from leaking through. The FULL ADDER is implemented using only three wavelengths which shows that the advantages of wavelength selective logic can be realized with a minimum number of channels. Although in Section IV, we predict that up to ten channels are possible within the tuning range of the WSOL, such a large number of channels requires high finesse optical cavities formed by regrowth of high reflectivity top mirrors and extreme accuracy in the overall growth and fabrication. Wavelength demultiplexing with three channels [21] has already been demonstrated within the RCE scheme, and should not pose any serious processing obstacles.

We can also imagine an optical storage element, which is the analog of an electrical FLIP FLOP, being fabricated from the WSOL device. Fig. 26 shows the proposed structure and internal feedback mechanism. Anisotropic etching can be used to create 45° surfaces which reflect part of the output signal back into the device which functions as a SET/RESET FLIP FLOP. This configuration exploits the capability of WSOL to represent each logic variable by a different wavelength by having each input element sensitive to the output wavelength of the other device. The WSOL scheme is flexible in that both local and global variables can be used. For instance, in synchronous sys-

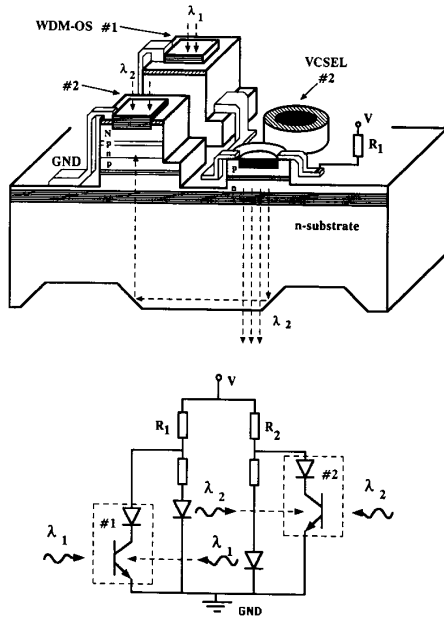


Fig. 26. Schematic representation of a wavelength selective optical storage element. Two distinct wavelengths are used for set and reset.

tems, a global clock wavelength can be broadcast over the entire system eliminating deleterious clock skew effects.

VII. CONCLUSION

We have proposed a novel wavelength selective optical logic (WSOL) circuit element, composed of monolithically integrated wavelength selective optical input and output elements, which is highly suitable for optical interconnect and logic applications. Input optical signals are detected by phototransistors situated in an optical cavity which provides a highly selective response at a wavelength determined by the fabrication process. Vertical cavity surface emitting lasers, whose lasing wavelengths can be tuned over a fairly broad range also determined by the fabrication process, provide a monochromatic output signal. The proposed vertical integration of these input and output elements will result in WSOL devices capable of detecting and emitting within a narrow designer selected wavelength range (not necessarily the same) at arbitrarily chosen positions across the wafer. The wavelength selectivity allows a large number of wavelengths to be used simultaneously while small crosstalk is maintained between the nearby devices. The WSOL device is highly suitable to optical interconnect applications. Since a single optical fiber can transmit all of the WSOL channels, the number of fibers required is reduced by a factor equal to the number of wavelength channels. This property significantly reduces the complexity and increases the reliability of optoelectronic signal conversion. WSOL elements can be configured to function as multiple variable logic gates. Examples of AND, OR, XOR, and HALF ADDER were presented. More complex arrangements such

as FULL ADDER and FLIP-FLOP for which the SET and RESET inputs can be specified at different wavelengths are also realizable. The WSOL device is suitable for integrated circuit applications so that arbitrarily complex logic operations will be possible.

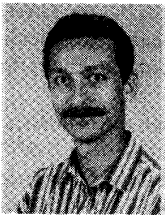
ACKNOWLEDGMENT

We would like to thank Dr. Y. Leblebici for valuable discussions.

REFERENCES

- [1] C. W. Wilmsen, S. A. Feld, F. R. Beyette, Jr., and X. An, "Switching light with light," *IEEE Circuits and Devices Mag.*, pp. 21-25, Nov. 1991.
- [2] K. Matsuda and J. Shibata, "Optical interconnections and optical computing based on the photonic parallel memory PPM," *IEE Proc. J.*, vol. 138, pp. 67-74, 1991.
- [3] J. E. Midwinter and M. G. Taylor, "Optoelectronic interconnects in VLSI: The reality of digital optical computing," *IEEE LCS Mag.*, pp. 40-46, May 1990.
- [4] T. Ikegami and H. Kawaguchi, "Semiconductor devices in photonic switching," *IEEE J. Selected Areas Commun.*, vol. 6, pp. 1131-1140, 1988.
- [5] H. Beneking, N. Grotem, W. Roth, and M. N. Svilane, "GaAs-GaAlAs phototransistor/laser light amplifier," *Electron. Lett.*, vol. 16, pp. 602-603, 1980.
- [6] M. S. Ünlü, S. Strite, A. Salvador, A. L. Demirel, and H. Morkoç, "Wavelength discriminating optical switch," *IEEE Photon. Technol. Lett.*, vol. 3, pp. 1126-1129, 1991.
- [7] G. W. Taylor, R. S. Mand, J. G. Simmons, and A. Y. Cho, "Optically induced switching in a p-channel double heterostructure optoelectronic switch," *Appl. Phys. Lett.*, vol. 49, pp. 1406-1408, 1986.
- [8] F. R. Beyette Jun, S. A. Feld, X. An, K. M. Geib, M. J. Hafich, G. Y. Robinson, and C. W. Wilmsen, "Integrated optical inverter using light amplifying optical switch (LAOS)," *Electron. Lett.*, vol. 27, pp. 497-499, 1991.
- [9] H. F. Lockwood, K.-F. Etzold, T. E. Stockton, and D. P. Marinelli, "The GaAs P-N-P-N laser diode," *IEEE J. Quantum Electron.*, vol. QE-10, pp. 567-569, 1974.
- [10] S. A. Feld, F. R. Beyette, Jr., M. J. Hofich, H. Y. Lee, G. Y. Robinson, and C. W. Wilmsen, "Electrical and optical feedback in InGaAs/InP light-amplifying switch (LAOS)," *IEEE Trans. Electron Dev.*, vol. 38, pp. 2452-2458, 1991.
- [11] P. Zhou, J. Cheng, S. Z. Sun, C. F. Schaus, C. Hains, D. R. Myers, and G. A. Vawter, "Surface-emitting laser-based optical bistable switching device," *Appl. Phys. Lett.*, vol. 59, pp. 2648-2650, 1991.
- [12] J. F. Gibbons, "Graphical analysis of the I-V characteristics of generalized p-n-p-n devices," *Proc. IEEE*, vol. 55, pp. 1366-1374, 1967.
- [13] —, "A critique of the theory of p-n-p-n devices," *IEEE Trans. Electron Dev.*, vol. 11, pp. 406-413, 1964.
- [14] F. E. Gentry, "Turn-on criterion for p-n-p-n devices," *IEEE Trans. Electron Dev.*, vol. ED-11, p. 74, 1964.
- [15] S. M. Sze, *Physics of Semiconductor Devices*. New York: Wiley, 1981, pp. 140-143.
- [16] K. Kishino, M. S. Ünlü, J.-I. Chyi, J. Reed, L. Arsenaull, and H. Morkoç, "Resonant cavity-enhanced (RCE) photodetectors," *IEEE J. Quantum Electron.*, vol. 27, pp. 2025-2034, Aug. 1991.
- [17] M. S. Ünlü, K. Kishino, J. I. Chyi, J. Reed, S. Noor Mohammad and H. Morkoç, "Resonant cavity enhanced AlGaAs/GaAs hetero-junction phototransistors with and intermediate InGaAs region in the collector," *Appl. Phys. Lett.*, vol. 57, pp. 750-752, 1990.
- [18] A. Chin and T. Y. Chang, "Multilayer reflectors by molecular beam epitaxy for resonance enhanced absorption in thin high-speed detectors," *J. Vac. Sci. Technol. B*, vol. 8, pp. 339-342, 1990.
- [19] R. H. Yan, R. J. Simes, and L. A. Coldren, "Analysis and design of surface-normal Fabry-Perot electrooptic modulators," *IEEE J. Quantum Electron.*, vol. 25, pp. 2272-2280, 1989.
- [20] M. S. Ünlü, K. Kishino, H. J. Liaw, and H. Morkoç, "A theoretical investigation of resonant cavity enhanced photodetectors with Ge and Si active regions," *J. Appl. Phys.*, vol. 71, pp. 4049-4058, 1992.
- [21] M. S. Ünlü, K. Kishino, J.-I. Chyi, J. Reed, L. Arsenaull, and H.

- Morkoç, "Wavelength demultiplexing heterojunction phototransistor," *Electron. Lett.*, vol. 26, no. 22, pp. 1857-1858, 1990.
- [22] H. Ishio, J. Minowa, and K. Nusu, "Review and status of wavelength-division-multiplexing technology," *J. Lightwave Technol.*, vol. LT-2, pp. 448-463, 1984.
- [23] R. P. Bryan, G. R. Olbright, W. S. Fu, T. M. Brennan, and J. Y. Tsao, "Near-infrared high-gain strained layer InGaAs heterojunction phototransistors: Resonant periodic absorption," *Appl. Phys. Lett.*, vol. 59, no. 13, pp. 1600-1602, 1991.
- [24] M. S. Ünlü, S. Taşiran, A. L. Demirel, and H. Morkoç, "Low-crosstalk monolithic wavelength demultiplexing switch arrays," *Proc., 1992 Bilkent Int. Conf. on Lightwave and Commun.*, Ankara, Turkey, July 27-28, 1992.
- [25] C. Chang-Hasnain, J. P. Harbison, C. Zah, and M. W. Maeda, L. T. Florez, N. G. Stoffel, and T.-P. Lee, "Multiple wavelength tunable surface emitting laser arrays," *IEEE J. Quantum Electron.*, vol. 27, pp. 1368-1375, 1991.
- [26] K. Iga, F. Koyama, and S. Kinoshita, "Surface emitting semiconductor lasers," *IEEE J. Quantum Electron.*, vol. 24, p. 1845, 1988.
- [27] P. B. Johnson and R. W. Christy, "Optical constants of the noble metals," *Phys. Rev. B*, vol. 6, pp. 4370-4379, 1972.
- [28] M. Mittelstein, D. Mehuys, A. Yariv, J. E. Ungar, and R. Sarfaty, "Broadband tunability of gain-flattened quantum well semiconductor lasers with an external cavity," *Appl. Phys. Lett.*, vol. 54, pp. 1092-1094, 1987.
- [29] J. T. Verdeyen, *Laser Electronics*. Englewood Cliffs, NJ: Prentice-Hall, 1981, pp. 53-75.

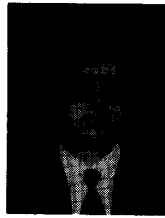


M. Selim Ünlü (S'90-M'92) was born in Sinop, Turkey, in 1964. He received the B.S. degree in electrical engineering from Middle East Technical University, Ankara, Turkey, in 1986, and the M.S.E.E. and Ph.D. in electrical engineering degrees from the University of Illinois, Urbana, in 1988 and 1992, respectively. His dissertation topic dealt with resonant cavity enhanced photodetectors and optoelectronic switches.

From 1984 to 1986, he was a part-time research engineer with Military Electronics Inc., Ankara, Turkey, where he worked on VHF communication systems. In 1992, he joined the Department of Electrical, Computer, and Systems Engineering, Boston University, Boston, MA, as an assistant professor. His current research interests are design, fabrication, characterization, and modeling of semiconductor electronic and optoelectronic devices.

Samuel Strite was born in Poughkeepsie, NY, in 1965. He received the B.S. degree in physics with honors from Bucknell University, Lewisburg, PA, in 1987.

Since then he has worked with the High Speed Device group at the University of Illinois under the direction of Hadis Morkoç. He has also worked on a wide variety of semiconductor systems including GaAs, Si, Ge, and GaN.



A. Levent Demirel (S'91) was born in Bursa, Turkey, in 1967. He received the B.S. degrees in electrical engineering and physics from Boğaziçi University, Istanbul, Turkey, in 1989 and the M.S. degree in physics from the University of Illinois, Urbana, in 1991.

He is currently working toward the Ph.D. degree in physics at the University of Illinois, Urbana. His research interests include the dynamics of confined liquids.

Serdar Taşiran was born in Turkey in 1970. He received the B.Sc. degree in electrical engineering from Bilkent University, Ankara, Turkey. He began his graduate studies at the University of Illinois, Urbana, in 1991. He is holding a NATO Science Fellowship for graduate study and is continuing his studies in electrical engineering at the University of California, Berkeley.

A. Salvador, photograph and biography not available at the time of publication.



Hadis Morkoç (S'72-M'76-SM'79-F'87) received the B.S.E.E. and M.S.E.E. degrees from Istanbul Technical University, Turkey, in 1968 and 1969, respectively. He began his Ph.D. studies at Michigan State University in 1971 and later transferred to Cornell University, NY, where he received the Ph.D. degree in electrical engineering in 1975. His dissertation topic dealt with liquid phase epitaxy of GaAs FET's.

He was with Varian Associates, Palo Alto, CA, from 1976 to 1978, where he was heavily involved in various novel FET structures. He has held visiting positions at AT&T Bell Laboratories (1978-1979), the California Institute of Technology, and the Jet Propulsion Laboratory (1987-1988). Since 1978, he has been with the University of Illinois pursuing research in heterostructure devices and materials. He has authored, coauthored, or edited *Principles and Technology of MODFETs*, 10 book chapters and proceedings, some 600 technical journal articles, 100 conference papers, and 40 technical reports. He has served as a consultant to some 15 industrial laboratories.

Dr. Morkoç is a Fellow of the American Association for the Advancement of Science, a Fellow of the American Physical Society, a member of the Material Research Society, a member of the Optical Society of America, a life member of Sigma Xi, a member of Eta Kappa Nu, and a life member of Phi Kappa Phi. He is listed in Who's Who in the Midwest American Men and Women in Science, Who's Who in Engineering, and International Men of Achievement. He received the ELECTRONIC LETTERS Best Paper Award in 1978 for his work in InGaAs FET's.